Prediction Of Geospace Radiation Environment and Solar wind parameterS

Work Package 5
Low energy electrons model improvements to develop forecasting products

Deliverable D5.1
Solar wind drivers of low energy plasmasheet electrons

N. Ganushkina, S. Dubyagin, I. Sillanpää
February 19, 2016

This project has received funding from the European Union's Horizon 2020 research and innovation programme under grant agreement No 637302

Document Change Record

Issue	Date	Author	Details
v3	21.12.2015	N. Ganushkina	
revised	19.02.2016	N.Ganushkina	revision after Reviewer's comments

Table of Contents

1. Introduction

The **Deliverable D5.1** entitled "Solar wind drivers of low energy plasmasheet electrons" is the first Deliverable of the **WP5** "Low energy electrons model improvements to develop forecasting products". The first objective of this WP is to develop an empirical solar wind and IMF driven model for low energy electrons in the plasma sheet. During the work under the Deliverable **D5.1**, the main focus was set at the **Task 5.1** "Developing a solar wind and IMF driven model for low energy electrons in the plasma sheet".

The distribution of low energy electrons, the seed population (10 to few hundreds of keV), is critically important for radiation belt dynamics. The source of these electrons is in the plasma sheet. Low energy electrons are followed in the Inner Magnetosphere Particle Transport and Acceleration model (IMPTAM) (*Ganushkina et al.*, 2013, 2014) from the plasma sheet at 10 Re to the inner magnetosphere regions. Therefore, it is crucially important to have accurate solar wind and IMF driven boundary conditions in the plasma sheet. The representation of kappa distribution function for electrons with number density n and temperature T parameters adapted from the empirical model derived from Geotail data by *Tsyganenko and Mukai* [2003] for ions with the same number density Te/Ti = 0.2 previously used in IMPTAM has a number of limitations. The main one is that it was developed for ions, not for electrons.

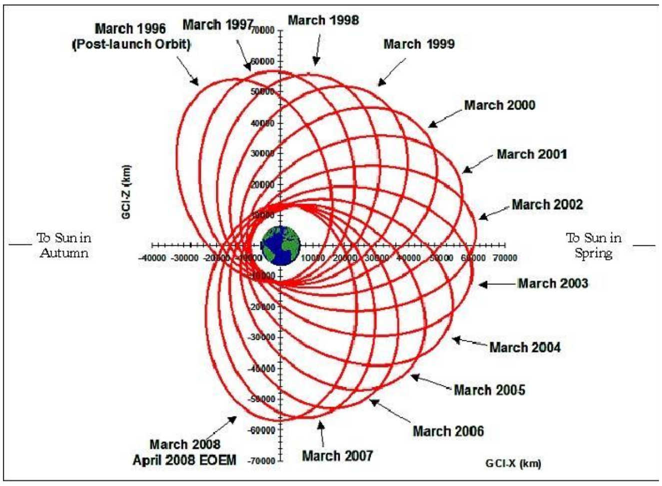

Figure 1. Precession of Polar satellite orbit.

A new empirical model for boundary conditions for low energy electrons at L=6-11 dependent on solar wind and IMF parameters is now constructed using the available satellite data on these distances. The empirical relations for plasma sheet electron number density and temperature during storm times are obtained based on the extensive analysis of THEMIS ESA (eV-30 keV) and SST (25 keV – 10 MeV) data during 2007-2013 (*Angelopoulos*, 2008; *McFadden et al.*, 2008). Choice of the THEMIS data as a primary data source came from the analysis of the best suited dataset.

Polar satellite orbit which had an apogee of 9 Re and 86 degrees of inclination in 1996, has precessed south with the inclination decrease at about 16 degrees per year (Figure 1). During the years of 2002 and 2003 the orbit was closest to the equatorial plane. The electron data from HYDRA DDEIS (10 eV-10 keV) (*Scudder at al.*, 1995) instrument could have been very useful for model construction but moments of electron distribution function are not available. At present, we are working with Dr. Reiner Friedel from LANL who has all the archived data and we hope to obtain the data during the duration of the project. These data will be used to further validate the constructed model.

Cluster spacecraft cross the plasma sheet and the data for electrons from **PEACE** (0.7 eV - 26 keV) (*Johnstone et al.*, 1997) instruments can be useful. At the same time, the close analysis of the orbit crossings revealed that Cluster sampled the regions located too far from the region of our interest (6-11 Re). For the Cluster magnetotail session in 2001-2005, we chose 70 orbits, which crossed the central plasma sheet at -16Re < Xgsm < -5Re and |Ygsm|<11Re. The central plasma sheet was identified as the region where |Bx| ≤ 5nT. Figure 2 presents the crossings in XY(GSM) and YZ(GSM) planes and most of them are at distances farther than 10 Re downtail. The dawn-dusk/north-south asymmetry of the plasma sheet crossings seen in Figure 2 is due to Cluster orbital/seasonal effect. Cluster apogee is in the dusk sector during September-October (when dipole tilt angle is predominantly 0 or >0) and it is on the dawnside during July-August (when dipole tilt angle is predominantly <0). Since the plasma sheet geometry is controlled by the Earth's magnetic dipole, the plasma sheet is offset in positive Z direction when dipole tilt angle is negative and vice versa. For this reason, Cluster plasma sheet crossings are at Z=0 or Z<0 in the dusk sector and at Z>0 on the dawnside. However, the plasma sheet plasma parameters do not depend on dipole tilt (as in *Tsyganenko and Mukai* [2003] model) and this dusk-dawn asymmetry does not have a significant effect. During the work under **Task 5.1**, Cluster data were used to demonstrate limitations of using *Tsyganenko and Mukai* [2003] model (developed for ions) for electrons.

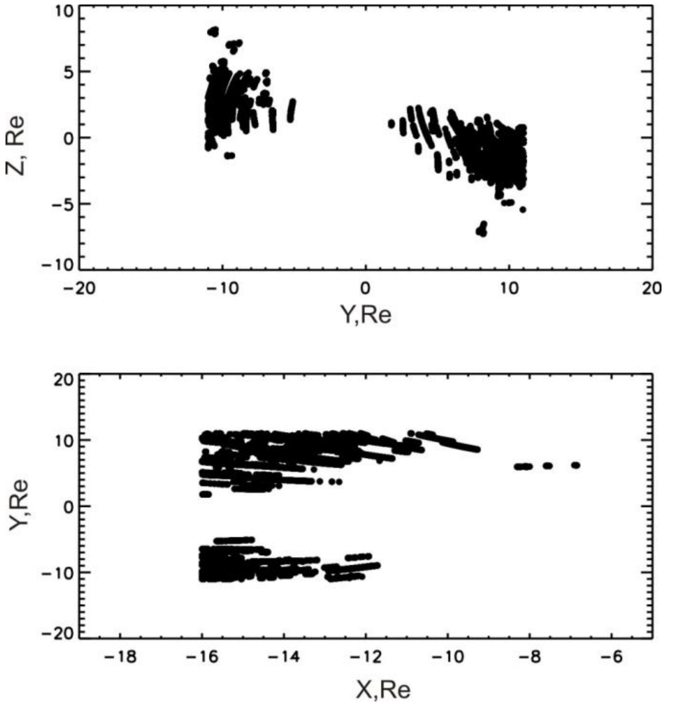

Figure 2. Cluster orbits crossing the plasma sheet.

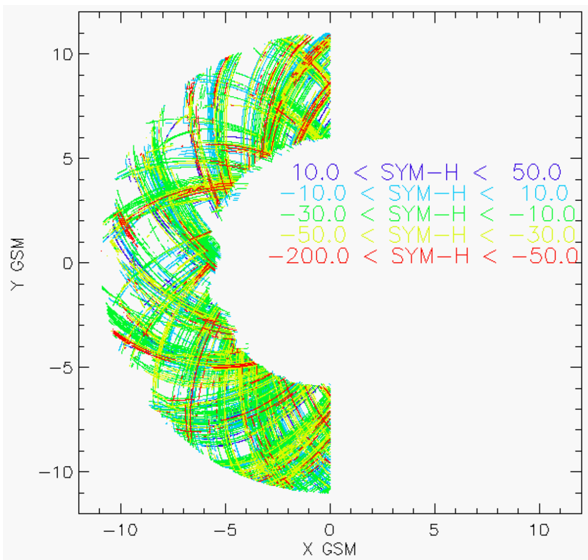

Figure 3. Distribution of the initially selected points (at 1min time resolution) in the XY GSM plane for different SYM-H indices.

THEMIS spacecraft had the best suitable orbit configurations for our model development. During 2008 and 2009 tail seasons (mid-December - April), apogees of all probes were lined up along the Earth's magnetotail within 2 Re along Ygsm-axis every fourth day (major conjunction), and four of the five were lined up every second day (minor conjunction). In the 2009 season, the three innermost probes (situated at about the same Xgsm) were separated along Ygsm and Zgsm by about 1 Re. During the extended phase (2010 - 2012), the innermost three spacecraft remained in nearly identical low-inclination orbits around Earth with geocentric apogees of 11.7 Re, orbital periods of 1 day, inclinations ranging from 1 to 8 deg. For the next extension, the probes remained at the 1-day orbit with gradually increasing separation (4-8-12 hrs in summer 2012, 8-8-8 hrs in summer 2014) along the track to support the NASA Van Allen Probes mission. To make sure that the probe was in the very center of the plasma sheet (near the magnetotail current neutral sheet) to refer the measurements to a particular radial distance, applied the approach described in *Dubyagin et al*. (2010). The data were calibrated and are publicly available at the THEMIS mission web site (http://themis.ssl.berkeley.edu/index.shtml). Figure 3 shows the distribution of the initially selected points (at 1-min time resolution) in the XY(GSM) plane. The times with SYM-H<-50 nT and one day before and one day after these periods were selected for the years of 2007-2013.

The empirical relations for electron plasma sheet density and temperature dependent on solar wind and IMF parameters are presented in the paper "Solar wind driven variations of electron plasma sheet densities and temperatures beyond geostationary orbit during storm times" by Dubyagin, S., N. Ganushkina, I. Sillanpää, A. Runov, V. Angelopoulos (ready for submission), below as a part of the **Deliverable D5.1** report.

At present, the model is being extensively validated by modeling several storm events using IMPTAM and comparing the modeled electron fluxes with the observed ones at Van Allen Probes (which are inside geostationary orbit) HOPE (20 eV-45 keV) data and geostationary measurements at GOES MAGED (40-150 keV), LANL MPA (3–45 keV) and SOPA (50-200 keV) (when available). Two papers are envisioned to be submitted early next year. This model has already been incorporated into IMPTAM. This is a significant improvement for the IMPTAM's ability to reproduce the low energy electron fluxes.

2. Conclusions

The empirical models of the plasma sheet electron temperature and density on the nightside for 6Re < r <11 Re are constructed based on THEMIS ESA and SST data. The plasma sheet electron density model dependence on external driving is parameterized by the solar wind proton density and southward IMF B_S component. The plasma sheet electron density shows stronger dependence on the southward IMF component averaged over preceding ~6 hour (storm main phase time-scale) rather than substorm growth phase time-scale. The electron perpendicular temperature model is parameterized by solar wind velocity and southward and northward components of IMF. In contrast to the electron density model, the electron temperature dependence on the southward IMF component is stronger when IMF B_S is averaged over preceding ~45 min (substorm growth phase time scale) lagged by ~30 min. The effect of the northward component has a longer lag (~1 hour) and ~2 hour duration. Model performance reveals the dawn-dusk asymmetry. The correlation (C.C.) between the model predictions and observations varies between C.C.>0.7 in the dawn MLT sector and C.C.= 0.4-0.5 in the dusk sector.

3. Future tasks and connection to other WPs

The IMPTAM with revised boundary conditions given by the newly developed empirical model in **Deliverable D5.1** will be used further throughout the project and for future Deliverables of **WP5**. In **Task 5.2** the diffusion coefficients provided by VERB radiation belts model with data assimilation extension from **Task 6.2** in **WP6** will be incorporated into IMPTAM. IMPTAM, in its turn, in **Task 5.3** will provide the low energy seed population to VERB radiation belts model. **Task 5.4** will result in developing of a trial version of forecast model for low energy electrons which will be part of **Task 7.2** in **WP7** for implementation of VERB-IMPTAM model in fusion of forecasting tools.

4. References

Angelopoulos, V, D. Sibeck, C. W. Carlson, et al., First Results from the THEMIS mission, *Space Sci. Rev.*, 141, 453-476, 2008.

Dubyagin, S., V. Sergeev, S. Apatenkov, et al., Pressure and entropy changes in the flow-braking region during magnetic field dipolarization, *J. Geophys. Res.*, 115, *A10225, doi:*10.1029/2010JA015625, 2010.

Ganushkina N. Yu., O. Amariutei, Y. Y. Shpritz, and M. Liemohn, Transport of the plasma sheet electrons to the geostationary distances, *J. Geophys. Res.*, 118, doi:10.1029/2012JA017923, 2013.

Ganushkina N. Yu., M. Liemohn, O. Amariutei, and D. Pitchford, Low energy electrons (5-50 keV) in the inner magnetosphere, *J. Geophys. Res.*, 119, 246259, 549 doi:10.1002/2013JA019304, 2014.

Johnstone A. D., C. Alsop, S. Burge, et al., Peace: A Plasma Electron and Current Experiment, *Space Sci. Rev.*, 79, 351-398, 1997.

McFadden, J.P., C.W. Carlson, D. Larson, et al., The THEMIS ESA Plasma Instrument and In-flight Calibration, *Space Sci. Rev.*, 141, 277-302, 2008.

Scudder, J., Hunsacker, F., Miller, et al., G.Hydra - A 3-Dimensional Electron and Ion Hot Plasma Instrument for the Polar Spacecraft of the GGS Mission, *Space Sci. Rev.*, 71, 459-495, 1995.

Tsyganenko, N. A., and T. Mukai, Tail plasma sheet models derived from Geotail particle data, *J. Geophys. Res.*, 108(A3), CiteID 1136, DOI 10.1029/2002JA009707, 2003.

Solar wind driven variations of electron plasma sheet densities and temperatures beyond geostationary orbit during storm times

S. Dubyagin[1], N. Yu. Ganushkina[1,2], I. Sillanpää[1], A. Runov[3],

V. Angelopoulos[3]

Corresponding author: S. Dubyagin, Finnish Meteorological Institute, POBox 503, Helsinki, FIN-00101, Finland/(Stepan.Dubyagin@fmi.fi)

[1]Finnish Meteorological Institute,

Helsinki, Finland.

[2]Climate and Space Sciences and

Engineering Department, University of

Michigan, Ann Arbor, MI, USA.

[3]Institute of Geophysics and Planetary

Physics, University of California,

Los Angeles, USA.

Abstract.

The empirical models of the plasma sheet electron temperature and density on the nightside for $6R_E <$ r <11 R_E is constructed based on THEMIS ESA and SST data. The plasma sheet electron density model dependence on external driving is parameterized by the solar wind proton density and southward IMF B_S component. The plasma sheet electron density shows stronger dependence on the southward IMF component averaged over preceding ∼6 hour (storm main phase time-scale) rather than substorm growth phase time-scale. The electron perpendicular temperature model is parameterized by solar wind velocity and southward and northward components of IMF. In contrast to the electron density model, the electron temperature dependence on the southward IMF component is stronger when IMF B_S is averaged over preceding ∼45 min (substorm growth phase time scale) lagged by ∼ 30 min. The effect of the northward component has a longer lag (∼1 hour) and ∼ 2 hour duration. Model performance reveals the dawn-dusk asymmetry. The correlation between the model predictions and observations varies between C.C.>0.7 in the dawn MLT sector and C.C.= 0.4–0.5 in the dusk sector.

1. Introduction

The distributions of low energy electrons (below 200-300 keV) and their variations in the near-Earth plasma sheet, at distances beyond geostationary orbit, have not sufficiently been studied in detail. Yet, this population is critically important for magnetospheric dynamics, especially during storm times. One obvious example is their role as the seed population, being further accelerated to MeV energies by various processes in the Earth's radiation belts. Several modeling attempts have been made [*Jordanova and Miyoshi*, 2005; *Miyoshi et al.*, 2006; *Chen et al.*, 2006; *Jordanova et al.*, 2014]. The electron flux at these low energies is largely determined by convective and substorm-associated electric fields and varies significantly with geomagnetic activity driven by the solar wind [*Mauk and Meng*, 1983; *Kerns et al.*, 1994; *Liemohn et al.*, 1998; *Ganushkina et al.*, 2013, 2014]. Inward electron transport includes also radial diffusion and excites plasma wave instabilities that give rise to local electron acceleration and electron precipitation into the atmosphere. Transport and loss processes are far from being understood at present. It should be also noted that the electron flux at these energies is important for surface charging [*Garrett*, 1981; *Lanzerotti et al.*, 1998; *Davis et al.*, 2008; *Thomsen et al.*, 2013].

There have been a number of studies on low energy electrons at geostationary orbit. *Korth et al.* [1999]; *Denton et al.* [2005]; *Sicard-Piet et al.* [2008]; *Denton et al.* [2015] concentrated mainly on the analysis of LANL MPA and SOPA electron data. *Friedel et al.* [2001] analyzed the electron data from the Polar Hydra instrument and *Kurita et al.* [2011] the data from the THEMIS spacecraft. None of the studies produced solar wind driven empirical relations for electron fluxes or moments of electron distribution function which can be used easily for radiation belt modeling. Moreover, to construct a model for keV electrons in the inner magnetosphere, the source for them, or the boundary conditions, needs to be set not at 6.6 R_E but in the near-Earth plasma sheet, at 10-12 R_E.

In the near-Earth plasma sheet, continuous measurements of plasma sheet electrons are not available, in contrast to geostationary orbit. Numerous studies addressed the magnetospheric plasma transport and sources [*Terasawa et al.*, 1997; *Borovsky et al.*, 1998a, b; *Wing and Newell*, 2002]. There have been several statistical models for plasma sheet electrons derived from GEOTAIL and CLUSTER data, such as, for example, *Borovsky et al.* [1997]; *Ebihara and Ejiri* [2000]; *Åsnes et al.* [2008]; *Burin des Roziers et al.* [2009]. *Artemyev et al.* [2013] analyzed the electron temperature radial distribution in the magnetotail using THEMIS observation at $r > 10R_E$. These studoes are not models with empirical relations which can be used for real event modeling by the wider scientific community.

Only two empirical models of the plasma sheet plasma parameters have been presented since 2000. These models are *Tsyganenko and Mukai* [2003] and *Sergeev et al.* [2015]. The *Tsyganenko and Mukai* [2003] model is the only model, where an analytical description of the plasma was derived for a 2D distribution of the central plasma sheet ion temperature T_i, density n_i and pressure p_i as functions of the incoming solar wind and interplanetary magnetic field parameters at distances of 10-50 R_E based on Geotail data. *Sergeev et al.* [2015] presented the correlations between 1-h-averaged central plasma sheet and solar wind (and AL index) parameters based on THEMIS data but they were not derived for storm times.

Ganushkina et al. [2013, 2014, 2015] modeled the electron transport from the plasma sheet to the geostationary orbit setting the boundary at 10 R_E as a kappa distribution with the parameters of number density n_e and temperature T_e in the plasma sheet given by *Tsyganenko and Mukai* [2003]. In *Ganushkina et al.* [2013, 2014, 2015], the electron n_e is assumed to be the same as that for ions and $T_e/T_i = 0.2$ is taken into account (as was shown, for example, in *Kaufmann et al.* [2005] and *Wang et al.* [2012], based on Geotail and THEMIS data). A time shift of 2 h following *Borovsky et al.* [1998b] for the solar wind material to reach the midtail plasma sheet is also introduced. Applying this model for boundary conditions for electrons has a number of serious limitations. The empirical model was derived from Geotail data for ions. According to the studies based on Geotail data analysis [*Wang et al.*, 2012], the ratio T_e/T_i can vary during disturbed conditions. Moreover, at distances closer than 10 R_E, it can happen that the correlation between T_i and T_e does not exist at all and no certain ratio can be determined [*Runov et al.*, 2015].

The paper presents the empirical model of the electron plasma sheet densities and temperatures derived from THEMIS [*Angelopoulos*, 2008a]. Sections 2 and 3 contain the detailed description of the data we have selected and analyzed. Section 4 demonstrates the methodology of determining the model input parameters. Section 5 presents the empirical relations for electron plasma sheet density and temperature. The goal of Section 6 is to validate the model performance and Section 7 presents the conclusions.

2. The Data

We have analyzed in details the data from particle detectors onboard the THEMIS probes P3, P4, P5 (D, E, A) during the epoch of 2007-2013 at distances beyond geostationary orbit up to 12 R_E. The Time History of Events and Macroscale Interaction during

Substorms (THEMIS) mission [*Angelopoulos*, 2008a], launched on February 17, 2007, employs five identical spacecraft on elliptical, nearly-equatorial orbits. Each of the probes has among other scientific instruments two particle instruments, namely, Electrostatic Analyser (ESA) [*McFadden et al.*, 2008] to measure the ion and electron distribution functions over the energy range from a few eV up to 25 (30) keV for ions (electrons) on each spin period (about 3 s) and Solid State Telescope (SST) [*Angelopoulos et al.*, 2008b] to measure ion and electron fluxes over energies from 25 keV up to first MeVs on each spin period. Although the combined distribution function covers the energy range up to 3 MeV we only used data in the 50 eV – 300 keV energy range. The plasma moments are publicly available at the THEMIS mission web site (http://themis.ssl.berkeley.edu/index.shtml) and they were computed using updated calibration procedures (including ESA background contamination and SST sun contamination, software version dated November 2015). We also used the spin resolution Flux Gate Magnetometer (FGM) data [*Auster et al.*, 1991].

In this study we used solar wind and IMF data from the OMNI database from the GSFC/SPDF OMNIWeb interface at http://omniweb.gsfc.nasa.gov. 5-min. resolution data were used as input parameters for magnetotail neutral sheet model [*Tsyganenko and Fairfield*, 2004] and 1-min. resolution data were used for computation of the input parameter for our empirical model of electron temperature and density.

Finally, the 1-min. resolution SYM-H index was downloaded from World Data Center for geomagnetism, Kyoto (http://wdc.kugi.kyoto-u.ac.jp/).

3. Selection of data intervals

We have analyzed all the time periods when the THEMIS probes were in the vicinity of the equatorial plane on the nightside (18-06 MLT). During 2008 and 2009 tail seasons (mid-December - April), apogees of all probes were lined up along the Earth's magnetotail within 2 R_E along Y-axis every fourth day (major conjunction), and four of the five were lined up every second day (minor conjunction). These spacecraft configurations enabled simultaneous monitoring of the mid-tail (X < -15 R_E) and near-Earth (X about -10 R_E) plasma sheet regions. In the 2009 season, the three innermost probes (situated at about the same X) were separated along Y and Z by about 1 R_E. During the extended phase (2010 - 2012), the innermost three spacecraft remained in nearly identical low-inclination orbits around Earth with geocentric apogees of 11.7 R_E, orbital periods of 1 day, inclinations ranging from 1 to 8 deg, and precession rates of 330deg/year. The probe separation in Y and Z directions varied between about 500 and 5000 km. During the next extension, the probes remained at the 1 day orbit with gradually increasing separation (4-8-12 hrs in summer 2012, 8-8-8 hrs in summer 2014) along the track to support the NASA Van Allen Probes mission.

Storm periods were of a special interest for our study, since the solar wind driving as well as magnetospheric plasma parameters can reach extreme values and all the dependencies as well as their saturation levels can manifest more clearly. For this reason, we selected all the periods with $SYM-H < -50$ nT and one day before and one day after these periods for almost whole THEMIS mission lifetime 2007–2013. This selection also includes the quiet periods before the storms.

When studying the distribution of the plasma parameters in the equatorial plane, it is important to make sure that a probe was in very center of the plasma sheet (near the magnetotail current neutral sheet) to refer the measurements to a particular radial distance. To control the spacecraft position relative to the neutral sheet we use two step selection: (1) Select all periods when the probes are within 1.5 R_E from the [*Tsyganenko and Fairfield*, 2004] model neutral sheet; (2) Using THEMIS magnetic field measurements we select only measurements when $|B_n| > |B_t|$, where B_n and B_t are the magnetic field components normal and tangential to the model neutral sheet. Such approach is very robust and it was successfully applied to the THEMIS data [*Dubyagin et al.*, 2010].

We then applied the aforementioned approach to select the points when the THEMIS P3, P4, P5 (D, E, A) probes were near the neutral sheet for $R = 6–11 R_E$. It was convenient to average the THEMIS $\sim$ 3 sec. plasma moments over 96 sec intervals ($\sim$ 1.6 minute). After synchronization with the solar wind data, we obtained $\sim 66,000$ data records. Figure 1a shows the distribution of the points in the XY_{GSM} plane (only every twentieth point is shown). The colors correspond to different $SYM-H$ index ranges.

It is worth comparing these datasets with datasets used in the previous studies. *Tsyganenko and Mukai* [2003] used Geotail data and their dataset comprised 7234 1-min records ($\sim$ 120 hours). Since we used 1.5-min resolution data, the size of our dataset should be multiplied by factor 1.5 to compare with *Tsyganenko and Mukai* [2003] dataset. However, we used observations onboard three probes clustered closely. For this reason, the size of our dataset should be divided by 3. After this normalization, our dataset size corresponds to $\sim$ 550 hours. *Wang et al.* [2006] apparently used the same data set as *Tsyganenko and Mukai* [2003]. *Sergeev et al.* [2015] use 4500–5000 hourly averaged measurements onboard three THEMIS probes on the nightside 21–06 MLT $r = 9–12 R_E$. After dividing by 3, to take into account simultaneous measurements at three probes, the data set size is 1500–1600 h, which is almost three times larger than data set used in the present study.

However, *Sergeev et al.* [2015] use only data from ESA spectrometer in 5 eV–25 keV energy range and there is no spatial dependance included in the model.

4. Solar wind driven model for electron plasma sheet densities and temperatures: Input parameters

4.1. Methodology

The macroscopic plasma parameters in the near-Earth magnetotail are affected by multiple factors. Among them, there are the magnetic configuration changes (it affects the plasma parameters through the adiabatic compression of the magnetic flux tubes) [*Artemyev et al.*, 2013; *Dubyagin et al.*, 2010; *Borovsky et al.*, 1998b], the substorm cycle (arrival of a new hot tenuous plasma from the distant magnetotail during the main phase) [*Sergeev et al.*, 2015], the variations of the magnetosheath plasma parameters (since it is a source of the plasma sheet material) [*Terasawa et al.*, 1997; *Borovsky et al.*, 1998a; *Wang et al.*, 2010], the variation of the magnetotail plasma transport modulated by the dayside reconnection rate. To make it even more complicated, the regions and mechanisms of the magnetosheath plasma penetration into the magnetotail are different during periods of southward and northward IMF [*Wang et al.*, 2010]. In addition, all these factors affect the plasma sheet with different time lags and these delays can be different for different regions of the magnetotail [*Terasawa et al.*, 1997; *Wang et al.*, 2010; *Borovsky et al.*, 1998a]

To investigate the lag of the solar wind influence, every record of the plasma sheet electron density and temperature was accompanied by solar wind data containing 12 hour prehistory. The solar wind parameters obtained from the OMNI database are referred to the time when solar wind reaches the estimated bow shock position. We estimate the shortest time for solar wind disturbance to has an effect on the nightside inner magnetosphere to be ~ 5 minutes. For every measurements in the plasma sheet taken at time t_0, the 12 hours period preceeding the time $t_0 - 5$ min. was broken into 15 minute intervals and solar wind parameters were averaged over these subintervals. That is, every measurement in the plasma sheet was complemented by 48 of 15-min averages of the solar wind parameters for the preceeding 12 h interval.

As a first step, we binned the THEMIS observations according to the probe location in the plasma sheet. We used two discriminating parameters: geocentric distance r and the azimuth angle $\phi = \arctan(-Y_{GSM}/Y_{GSM})$. We used two intervals of geocentric distance: r = 6–8.5R_E and r = 8.5–11R_E, and three sectors of the azimuth angle: dawnside ($-90° < \phi < -30°$), central ($30° < \phi < 30°$), and duskside ($30° < \phi < 90°$). These bins are shown in Figure 1b. We investigated the dependance of the electron plasma parameters on solar wind parameters separately for each bin. Let P_k be a plasma sheet parameter and D_{ik} are 15-min averages of some solar wind parameter. Here k is the index corresponding to the plasma sheet measurements at the time t_k and $i = 1, ..., 48$ corresponds to the 15-min average delayed by $\Delta t = 5 \text{ min} + i \cdot 15$ min. with respect to the time t_k.

For $L = 1, ..., 48$ and for $M < 48 - L$, we computed the following mean sums:

$$F(L, M, k) = \frac{\sum_{i=L}^{M} D_{ik}}{M}. \quad (1)$$

Here L represents a lag and M represents duration over which the parameter is averaged. These sums are equivalent to time integrals:

$$F(t_{lag}, \Delta T, t_k) = \frac{1}{\Delta T} \int_{t_k - t_{lag} - \Delta T}^{t_k - t_{lag}} D(t) dt. \quad (2)$$

The delays of the plasma sheet parameter response to the changes of the solar wind can be deduced from analysis of the correlation coefficient between P_k and $F(L, M, k)$ for different L and M. These correlation coefficients can be plotted as function of L and M converted to the time units t_{lag} and ΔT.

Imagine an ideal system whose parameter P responds to the changes of some other parameter D with a fixed lag t_r. The correlation between P and D will have a peak at $t_{lag} = t_r$ and $\Delta T = 0$. However, the correlation will still be high for ΔT which are less than some fraction of the D-autocorrelation time scale T_{auto} (that is, if an instant value of D can be approximated by its mean average over the time interval ΔT) under condition that t_r is inside of the ΔT interval ($t_{lag} < t_r < t_{lag} + \Delta T$). The shaded area in Figure 2 shows the region satisfying the aforementioned conditions. Obviously, inside this region the correlation is highest when the interval of averaging is centered at t_r, that is $t_{lag} + \Delta T/2 = t_r$ (blue dashed line in Figure 2).

However, the parameters of the system not necessarily depend on instant values (even if lagged) of the external drivers. For example, the magnetic flux in the magnetotail lobes better correlates with a time integrated solar wind geoeffective electric field than with its instant value. In such a case, one can expect that correlation would be higher at $\Delta T \neq 0$. In addition, in real magnetosphere the time lags obviously are not constant. It also leads to smearing out the correlation peak at $\Delta T = 0$ and an increase of the correlation at $\Delta T \neq 0$.

4.2. Input parameters for electron plasma sheet density model

Figure 3 shows the plots for correlation between the plasma sheet and solar wind densities. Figures 3a–f correspond to six spatial bins shown in Figure 1b. The horizontal axis corresponds to the time lag or index L in Equation 1. The vertical axis corresponds to the interval of averaging or index M in Equation 1. A color scale on the right side of each plot shows the range of the linear correlation coefficients (C.C.).

There is an obvious similarity between these plots and Figure 2. The correlation maximum in Figures 3a, b, d, e are organized along lines $\Delta T_N = const - 2 \cdot t_N$, and the regions of enhanced correlation are delineated by lines $\Delta T_N = const - t_N$ on the left/bottom side.

The plots on the left and right correspond to the dawn and dusk bins. It can be seen that the maximum correlation is found for the duskside bins (C.C.$\approx$ 0.6–0.75) and the correlation is higher for the outer bins (BIN 1–3 see Figure 1b). It can be seen, that for a given ΔT_N, the maximum correlation for the duskside bins is achieved for larger t_N in comparison to the dawnside bins. On one hand, these results are in agreement with dusk-dawn asymmetry of the plasma transport form the magnetosheath found by *Wing et al.* [2005]; *Wang et al.* [2010], however, it is a bit counterintuitive taking into account the eastward direction of the electron magnetic drifts. The lag values are generally in agreement with those found by *Borovsky et al.* [1998a]. The peak of the correlation at $t_N > 10$ h, which is seen in Figure 3f, is likely due to the electrons drifting around the Earth and coming to the BIN 6 from the dayside (BIN 6 is on the dusk flank near geosynchronous orbit). This delay ($\sim$ 12 hours) correspond to that found by *Borovsky et al.* [1998a] for solar wind - dayside geosynchronous orbit lag (see their Figure 11).

Table 1 presents the statistical properties of the datasubsets for the different bins. Forth line shows the number of 1.5-min resolution records in every bin. It can be seen that the most sparsely populated bin is BIN 6. Its data set comprises 7873 records that is equivalent to $\sim$65 hours of observations. The BIN 1 data set is more than two times larger. It is not much in comparison to the duration of the 12-hour prehistory interval. For this reason (and may be partly due to orbital/seasonal effect), the standard deviations of the solar wind parameters also show some variations from bin to bin. Bottom part of the Table 1 shows the ranges of the standard deviations found for various lag values between 0 and 12 hours. It can be seen that the variability of the solar wind parameters changes a lot for different time lag values inside a datasubset for a single bin. It means that some dependencies seen in Figure 3 could be due to limited size of the dataset since it is expected that correlation coefficient between two quantities depends on the standard deviation. To rule out this possibility, we plotted additional figures (not shown) in the same format as Figure 3 but for a standard deviation of a corresponding solar wind parameter. Analyzing these figures, we found that the main features seen in Figures 3a, b, d, e are real (σ shows no variation in that part of the figure). However, an increase of the correlation in the left bottom corner of Figure 3c (for $t_N < 4$ h) as well as in the middle part of Figure 3f (3 h $< t_N <$ 6 h and $\Delta T_N <$ 4 h) can be due to an increased standard deviation of N_{SW} in those regions of the plot.

Although the values of ΔT_N and t_N corresponding to the highest correlation obviously depend on azimuthal angle and radial distance, we need to choose the fixed values for computation of the input parameters for empirical models. Although the highest correlations were found for the duskside bins, we attempted to find a compromise so that the model works for all MLTs in $r = 6$–$11 R_E$ range. Keeping this in mid, we chose $t_N = 1.5$ h and $\Delta T_N = 3.5$ h.

Figure 4 shows the plots of correlations between the plasma sheet electron density and southward component of the IMF B_Z (B_S). The format is the same as in Figure 3. In contrast to the solar wind density, the highest correlation between the B_S and plasma sheet electron density is found for the near-Earth bins. Surprisingly, highest correlations are obtained for relatively long interval of averaging $\Delta T_{BS} = 2$–6 h. This is much longer than typical substorm growth phase duration. It could be due to strong variations of the lag in the real system, but in such a case one would expect weaker correlation. Although having no an explanation for this finding, we chose the $t_{BS} = 1.33$ h and $\Delta T_{BS} = 5.5$ h.

Table 2 summarizes the results presented in this section. When comparing the top and bottom parts of the Table 2, it can be seen that introducing a time lag to the input parameter significantly improves the correlations. It can be noticed that northward component of IMF shows worse correlation than N_{SW} and IMF B_S. We have also checked a few more solar wind and IMF parameters (not shown). However, even if the correlations were comparable to those for N_{SW} and B_S, the resulting model quality (see Section 6) was worse and we discarded them in the present version of the model. For example, motivated by the fact that the solar wind - magnetotail plasma transport characteristic time is different for the intervals southward and northward IMF B_Z, we introduced two parameters $N_{SW}^{(S)}$ and $N_{SW}^{(N)}$. $N_{SW}^{(S)} = N_{SW}$ when IMF $B_Z < 0$ and $N_{SW}^{(S)} = 0$ when IMF $B_Z > 0$. Opposite is true for $N_{SW}^{(N)}$. Although the lag-duration plots showed plausible patterns, the resulting quality of the electron density model was worse. For this reason, we have left N_{SW} and B_S as imput parameters of our model.

4.3. Input parameters for electron plasma sheet temperature model

Table 3 shows the correlation between the plasma sheet electron perpendicular temperature (T_e) and solar wind parameters. It can be seen that solar wind velocity exhibits strongest correlation. Similar results have been found for plasma sheet ion temperature

[*Borovsky et al.*, 1998a; *Tsyganenko and Mukai*, 2003]. It can also be noticed that IMF B_S and B_N affect the electron temperature in an opposite way. Figure 5 shows the correlations between T_e and V_{SW} for six spatial bins in the same format as in Figure 3. The highest correlations are obtained for the duskside bins. The correlations show very weak dependence on t_V and ΔT_V. It is expected result since the solar wind velocity autocorrelation characteristic time scale is largest of all solar wind parameters (See Figure 6 in *Borovsky et al.* [1998a]). We almost arbitrary chose $t_V = 0.5$ h and $\Delta T_V = 1$ h.

Figure 6 shows the similar correlation plots for IMF B_S. There is no clear dependence on MLT. Although for some bins the correlation is rather weak, the duration and the lag at the correlation peak fit well the substorm timescales: the time lag $t_{BS} = 30$ minutes can be interpreted as the time needed for the lobe magnetic flux to start to influence the near-Earth magnetotail and the averaging interval $\Delta T_{BS} = 45$ minutes is close to the typical substorm growth phase duration.

Figure 7 shows the similar plots for IMF B_N. Color scale on the right side of each plot corresponds to the absolute value of the correlation coefficient. The highest correlation is on the duskside. Surprisingly, the correlations are even higher than those for B_S. To make sure that these correlations are not due to the mutual correlation between IMF B_N and V_{SW}, we inspected the correlation between B_N and V_{SW} for various lags t_V and t_{BN} and found no significant correlation. We chose $t_{BN} = 0.58$ h and $\Delta T_{BN} = 2$ h.

5. Solar wind driven model for electron plasma sheet densities and temperatures: Empirical relations

Using the time constant determined in the previous section (Table 4) we computed the input parameters for the electron density and temperature models. At the first step, we use the following functional form of the plasma sheet parameter dependence on the solar wind input parameters:

$$P_{ps} = G_0(\phi, R) + \sum_{j=1,...} G_j(\phi, R) \cdot P_j^{SW}, \quad (3)$$

where P_j^{SW} are the corresponding solar wind parameters, and $G_j(\phi, R)$ are the 2nd order polynomials of an azimuth angle and radial distance given as

$$G_j(\phi, R) = \sum_{m,n=0,1,2} C_{mnj} \cdot R^n \phi^m. \quad (4)$$

The polynomial coefficients were found by fitting Equation 3 to the data. After the first set of the coefficients was found, we computed the correlation coefficient between the plasma sheet parameters and the model predictions. Using this correlation coefficient as a reference value, we varied combinations of the free parameters (simplifying the polynomials) excluding those terms which turned out to be insignificant. That is, for every combination of the free parameters, we fitted the model to the data and computed the correlation coefficient between the data and the model. Comparing this coefficient with a reference one we made sure that the removal of these terms from Equation 3 did not lead to significant reduction of the model quality.

Applying this method to the plasma sheet electron density and temperature datasets, we come up with following solutions. The number density in the plasma sheet (N_{ps}) is given in cm^{-3} as follows:

$$N_{ps} = A_1 + A_2\phi^* + A_3\phi^{*2} + (A_4 + A_5\phi^*)N_{sw}^* + (A_6 + A_7R^*){B_S^*}^{A_8}, \quad (5)$$

where N_{sw}^*, B_S^* are the time-integrated and normalized parameters characterizing the external conditions and defined as:

$$N_{sw}^*(t_0) = \frac{1}{10 \text{ cm}^{-3} \Delta T_N} \int_{t_0-t_N-\Delta T_N}^{t_0-t_N} N_{sw}(t)dt, \quad (6)$$

$$B_S^*(t_0) = \frac{1}{2 \text{ nT } \Delta T_{BS}} \int_{t_0-t_{BS}-\Delta T_{BS}}^{t_0-t_{BS}} B_S(t)dt. \quad (7)$$

Here, N_{sw} and B_S are the solar wind density and southward IMF component. The values for t_N, ΔT_N, t_{BS} and ΔT_{BS} are given in Table 4 and the model coefficients A_i are given in Table 5.

The temperature in the plasma sheet (T_{ps}) is given in keV as follows:

$$\begin{aligned} T_{ps} = [&A_1 + A_2R^* + A_3\phi^* + A_4\phi^*R^* + A_5\phi^{*2}R^* + \\ &+(A_6R^* + A_7\phi^{*2} + A_8\phi^{*2}R^*)V_{sw}^* + \\ &+A_9\phi^*{B_S^*}^{A_{11}} + A_{10}R^*{B_N^*}^{A_{12}}]^2, \end{aligned} \quad (8)$$

where

$$V_{sw}^*(t_0) = \frac{1}{400 \text{ km/s } \Delta T_V} \int_{t_0-t_V-\Delta T_V}^{t_0-t_V} V(t)dt, \quad (9)$$

$$B_S^*(t_0) = \frac{1}{2 \text{ nT } \Delta T_{BS}} \int_{t_0-t_{BS}-\Delta T_{BS}}^{t_0-t_{BS}} B_S(t)dt, \quad (10)$$

$$B_N^*(t_0) = \frac{1}{2 \text{ nT } \Delta T_{BN}} \int_{t_0-t_{BN}-\Delta T_{BN}}^{t_0-t_{BN}} B_N(t)dt. \quad (11)$$

Here, V_{sw}, B_S, and B_N are the solar wind density and the southward and northward IMF components, respectively. The values for t_V, ΔT_V, t_{BS}, ΔT_{BS}, t_{BN} and ΔT_{BN} are given in Table 4 and the model coefficients A_i are given in Table 5.

It can be seen that the plasma sheet electron density dependence on the solar wind density is stronger on the dawn flank. It is probably due electron eastward magnetic drift. On the contrary, the dependence on the IMF B_S is stronger in the near-earth region.

6. Solar wind driven model for electron plasma sheet densities and temperatures: Model performance

Figures 8 and 9 present the scatter plots of the model predictions versus real THEMIS observation for electron density and temperature models, respectively. The correlation coefficients between the model and the data were 0.76 for electron density and 0.65 for electron temperature models. Table 6 shows the correlation coefficients between the model predictions and the real data computed separately for every spatial bin. The root-mean-square deviations (RMS) and mean absolute deviations (MAD) are also shown. It can be seen that both models show their best performance on the dawnside of the region. It is not immediately clear what causes such asymmetry. Since the electrons undergo eastward magnetic drifts, their drift trajectories are expected to be regular on the dawnside, in contrast to the duskside where the drift paths can bifurcate (especially in the near-Earth region). Substorm activity is typically peaked at the pre-midnight sector (and this distortion can become even stronger during the storm periods) and it can also contribute to the poor performance of the model on the duskside.

Analyzing the coefficients in Table 5, it can be seen that the model dependencies on solar wind driving parameters vary over the region of the magnetotail. The plasma sheet electron density response to the solar wind density changes is positive and strongest on the dawnside ($\sim$ 2 times stronger on the dawnside in comparison to duskside).

It a bit surprising, but the electron density response to the southward IMF component is also positive. However, it should be remembered that the model is parameterized by B_S lagged by 1.3 h and averaged over almost six hours, that is, this density response is not related to the substorm cycle but rather to geomagnetic storm time-scale. This response is strongest in the near-Earth region and disappears at $r = 11R_E$. It can be interpreted as a result of the compression of the flux tube due to inflation of the inner magnetosphere magnetic configuration caused by the ring current strengthening.

The electron temperature increases with the solar wind velocity increase throughout the region of the model applicability. At the outer boundary of the model ($r = 11R_E$), this response is strongest in the central part and somewhat weaker at the dawn and dusk MLT sectors. This MLT-dependence almost disappears at the inner boundary ($r = 6R_E$). The coefficient at V^*_{SW} is $\sim$ 2 times smaller at ($r = 6R_E$) than at ($r = 11R_E$, MLT= 0 h).

The electron temperature response to the southward IMF component reveals dawn-dusk asymmetry. The temperature increases with B_S in the dawn MLT sector and shows opposite dependance on the dusk side. The electron temperature response to the northward IMF component (integrated over 2 hours) is negative. It is probably related to the arrival of the cold magnetosheath plasma during the intervals of the northward IMF [*Wing et al.*, 2005; *Wang et al.*, 2007, 2010]. This hypothesis is also confirmed by the fact that the effect is $\sim$ 2 times stronger at $r = 11R_E$ than at $r = 6R_E$. On the other side, it is expected that the effect is stronger at the flanks of the magnetosphere but we found no clear dependence on MLT.

Comparison of our models performance with other empirical models is not straightforward. On one hand, our electron density model shows the best correlations between the model predictions and the data. On the other hand, such an evaluation of the model performance is strongly biased. The regions of applicability of the models overlap only partly. The different datasets were used for the construction of the models. Our dataset mostly includes storm-time intervals. The solar wind driving parameters undergo stronger variations during storm periods and all dependencies can be tracked more easily. On the other side, these highly disturbed periods obviously add more scatter to the data.

Tsyganenko and Mukai [2003] ion temperature model has somewhat higher correlation than our model for electron temperature (0.71 versus 0.65). It should be mentioned that the correlations were computed for the whole region of the model applicability. Since the *Tsyganenko and Mukai* [2003] model covers the magnetotail between $r = 10$–$50 R_E$, and the ion temperature reveals a stable increase with distance, a simple comparison of the correlations for the whole datasets puts the *Tsyganenko and Mukai* [2003] model in the more favorable conditions. In addition, *Runov et al.* [2015] found that the correlation between the ion and electron temperatures disappears at $r < 12 R_E$.

For development in the future we foresee the following possibilities: (1) Possible presence of the multiple population components (cold, hot) should be addressed; (2) The inclusion of the geomagnetic activity indices as input parameters will increase the model accuracy; (3) Expansion of the dataset including non-storm periods.

7. Conclusions

The empirical models of the plasma sheet electron temperature and density on the nightside for $6R_E < r < 11R_E$ has been constructed. The models depend on spatial coordinates as well as on the external conditions. The plasma sheet electron density model dependence on external driving is parameterized by the solar wind proton density and southward IMF B_S component. In agreement with results of previous studies, the solar wind proton density is the main controlling parameter but the IMF B_S becomes of almost the same importance in the near-Earth region ($r 6.6R_E$).

The model performance has been essentially improved by using lagged and time averaged solar wind parameters as model input. The best time-lag and duration of average values were different for different parameters as well as showed some dependance on MLT (not included in the current model version). The plasma sheet electron density shows stronger dependence on the southward IMF component averaged over preceding ∼6 hour (storm main phase time-scale) rather than substorm growth phase time-scale.

The electron perpendicular temperature model is parameterized by solar wind velocity and southward and northward components of IMF. The solar wind velocity is a major controlling parameter and the importance of B_S and B_N is comparable.

In contrast to the density model, the electron temperature dependence on the southward IMF component is stronger when IMF B_S is averaged over preceding ∼45 min (substorm growth phase time scale) lagged by ∼ 30 min. The effect of the northward component has a longer lag (∼1 hour) and ∼ 2 hour duration.

Model performance reveals the dawn-dusk asymmetry. The correlation between the model predictions and observations varies between C.C.>0.7 in the dawn MLT sector and C.C.= 0.4–0.5 in the dusk sector.

Acknowledgments.

The plasma moments were obtained from the THEMIS mission web site (http://themis.ssl.berkeley.edu/index.shtml). The solar wind and IMF data were downloaded from the OMNI database from the GSFC/SPDF OMNIWeb interface at http://omniweb.gsfc.nasa.gov. The 1-min. resolution SYM-H index was provided by the World Data Center for geomagnetism, Kyoto (http://wdc.kugi.kyoto-u.ac.jp/). The part of the research done by N. Ganushkina and S. Dubyagin has received funding from the European Union Seventh Framework Programme (FP7/20072013) under grant agreement 606716 SPACESTORM and from the European Union Horizon 2020 Research and Innovation programme under grant agreement 637302 PROGRESS. N. Ganushkina thanks the International Space Science Institute in Bern, Switzerland, for their support of the international teams on "Analysis of Cluster Inner Magnetosphere Campaign data, in application the dynamics of waves and wave-particle interaction within the outer radiation belt" and "Ring current modeling: Uncommon Assumptions and Common Misconceptions".

References

Artemyev, A. V., Petrukovich, A. A., Nakamura, R., and Zelenyi, L. M. (2013), Profiles of electron temperature and Bz along Earth's magnetotail, *Ann. Geophys.*, *31*, 1109–1114, doi:10.5194/angeo-31-1109-2013.

Auster, H. U., et al. (2008), The THEMIS fluxgate magnetometer, *Space Sci. Rev.,*, *141*, 235–236, doi: 10.1007/s11214-008-9365-9.

Angelopoulos, V. (2008a), The THEMIS mission, *Space Sci. Rev.*, *141*, 5-34, doi:10.1007/s11214-008-9336-1.

Angelopoulos, V, D. Sibeck, C.W. Carlson, et al. (2008b), First Results from the THEMIS mission, *Space Sci. Rev.*, *141*, 453-476.

Borovsky, J. E., Thomsen, M. F., McComas, D. J. (1997), The superdense plasma sheet: Plasmaspheric origin, solar wind origin, or ionospheric origin?, *J. Geophys. Res.*, *102(A10)*, 22089.

Borovsky, J. E., M. F. Thomsen, and R. C. Elphic (1998a), The driving of the plasma sheet by the solar wind, *J. Geophys. Res.*, *103(A8)*, 17617-17639, doi:10.1029/97JA02986.

Borovsky, J. E., M. F. Thomsen, R. C. Elphic, T. E. Cayton, and D. J. McComas (1998b), The transport of plasma sheet material from the distant tail to geosynchronous orbit, *J. Geophys. Res.*, *103(A9)*, 20297-20331, doi:10.1029/97JA03144.

Burin des Roziers, E., X. Li, D.N. Baker, T.A. Fritz, R. Friedel, T.G. Onsager, and I. Dandouras (2009), Energetic plasma sheet electrons and their relationship with the solar wind: A cluster and geotail study, *J. Geophys. Res.*, *114*, A02220, DOI: 10.1029/2008JA013696.

Chen Y., R. H. W. Friedel, G. D. Reeves, PSD distributions of energetic electrons in the outer radiation belt during two Geospace Environment Modeling Inner Magnetosphere/Storms selected storms, *J. Geophys. Res.*, *111*, A11S04, doi:10.1029/2006JA011703, 2006.

Davis, V. A., M. J. Mandell, and M. F. Thomsen (2008), Representation of the measured geosynchronous plasma environment in spacecraft charging calculations, *J. Geophys. Res.*, *113*, A10204, doi:10.1029/2008JA013116.

Denton, M. H., M. F. Thomsen, H. Korth, S. Lynch, J. C. Zhang, and M. W. Liemohn (2005), Bulk plasma properties at geosynchronous orbit, *J. Geophys. Res.*, *110*, A07223, doi:10.1029/2004JA010861.

Denton, M. H., M. F. Thomsen, V. K. Jordanova, M. G. Henderson, J. E. Borovsky, J. S. Denton, D. Pitchford, and D. P. Hartley (2015), An empirical model of electron and ion fluxes derived from observations at geosynchronous orbit, *Space Weather*, *13*, doi:10.1002/2015SW001168.

Dubyagin, S., V. Sergeev, S. Apatenkov, V. Angelopoulos, R. Nakamura, J. McFadden, D. Larson, and J. Bonnell (2010), Pressure and entropy changes in the flow-braking region during magnetic field dipolarization, *J. Geophys. Res.*, *115*, A10225, doi:10.1029/2010JA015625.

Ebihara, Y., and Ejiri, M. (2000), Simulation study on fundamental properties of the storm-time ring current, *J. Geophys. Res.*, *105*, 15,843.

Friedel, R. H. W., H. Korth, M. G. Henderson, M. E. Thomsen, J. D. Scudder (2001), Plasma sheet access to the inner magnetosphere, *J.* Geophys. Res., *1*06, 5845-5858.

Jordanova, V. K., and Y. S. Miyoshi (2005), Relativistic model of ring current and radiation belt ions and electrons: Initial results, *Geophys. Res. Lett.*, *32*, L14104, doi:10.1029/2005GL023020.

Jordanova, V. K., Y. Yu, J. T. Niehof, R. M. Skoug, G. D. Reeves, C. A. Kletzing, J. F. Fennell, and H. E. Spence (2014), Simulations of inner magnetosphere dynamics with an expanded RAM-SCB model and comparisons with Van Allen Probes observations, *Geophys. Res. Lett.*, *41*, 2687-2694, doi:10.1002/2014GL059533.

Ganushkina N. Yu., O. Amariutei, Y. Y. Shpritz, and M. Liemohn (2013), Transport of the plasma sheet electrons to the geostationary distances, *J.* Geophys. Res., *118*, doi:10.1029/2012JA017923.

Ganushkina N. Yu., M. Liemohn, O. Amariutei, and D. Pitchford (2013b), Low energy electrons (5-50 keV) in the inner magnetosphere, *J.* Geophys. Res., 119, 246259, doi:10.1002/2013JA019304.

Ganushkina, N. Y., O. A. Amariutei, D. Welling, and D. Heynderickx, (2015), Nowcast model for low-energy electrons in the inner magnetosphere, *S*pace Weather, *1*3, 1634, doi:10.1002/2014SW001098.

Garrett, H. B. (1981), The charging of spacecraft surfaces, *R*ev. Geophys., *1*9(4), 577, doi:10.1029/RG019i004p00577.

Kaufmann, R. L., W. R. Paterson, and L. A. Frank (2005), Relationships between the ion flow speed, magnetic flux transport rate, and other plasma sheet parameters, *J.* Geophys. Res., *1*10, A09216, doi:10.1029/2005JA011068.

Kerns, K. J., D. A. Hardy, and M. S. Gussenhoven, Modeling of convection boundaries seen by CRRES in 120-eV to 28-keV particles, *J.* Geophys. Res., *9*9, 2403, 1994.

Korth, H., M. F. Thomsen, J. E. Borovsky, and D. J. McComas (1999), Plasma sheet access to geosynchronous orbit, *J.* Geophys. Res., *1*04, 25,047-25,061.

Kurita, S., Y. Miyoshi, F. Tsuchiya, Y. Nishimura, T. Hori, Y. Miyashita, T. Takada, A. Morioka, V. Angelopoulos, J. P. McFadden, H. U. Auster, J. M. Albert, V. Jordanova, and H. Misawa et al. (2011), Transport and loss of the inner plasma sheet electrons:

THEMIS observations, *J.* Geophys. Res., *1*16, A03201, doi:10.1029/2010JA015975.

Lanzerotti, L. J., K. LaFleur, C. G. Maclennan, and D. W. Maurer (1998), Geosynchronous spacecraft charging in January 1997, *Geophys. Res. Lett.*, *25(15)*, 2967-2970.

Liemohn, M. W., G. V. Khazanov, and J. U. Kozyra (1998), Banded electron structure formation in the inner magnetosphere, *G*eophys. Res. Lett., *2*5, 877.

Mauk, B. H., and C.-I. Meng (1983), Characterization of geostationary particle signatures based on the "Injection Boundary" model, *J.* Geophys. Res., *8*8, 3055.

McFadden, J. P., Carlson, C. W., Larson, D., Angelopoulos, V., Ludlam, M., Abiad, R., Elliott, B., Turin, P., Marckwordt, M. (2008), The THEMIS ESA plasma instrument and in-flight calibration, *Space Sci. Rev., 141*, 277–302, doi: 10.1107/s11214-008-9440-2

Miyoshi, Y. S., V. K. Jordanova, A. Morioka, M. F. Thomsen, G. D. Reeves, D. S. Evans, and J. C. Green (2006), Observations and modeling of energetic electron dynamics during the October 2001 storm, *J. Geophys. Res.*, *111*, A11S02, doi:10.1029/2005JA011351.

Ohtani, S., and T. Mukai (2008), Statistical characteristics of the storm time plasma sheet, *J. Geophys. Res.*, *113*, A01221, doi:10.1029/2007JA012547.

Runov, A., V. Angelopoulos, C. Gabrielse, J. Liu, D. L. Turner, and X.-Z. Zhou (2015), Average thermodynamic and spectral properties of plasma in and around dipolarizing flux bundles. *J. Geophys. Res. Space Physics*, *120*, 4369-4383, doi:10.1002/2015JA021166.

Sergeev, V. A., N. P. Dmitrieva, N. A. Stepanov, D. A. Sormakov, V. Angelopoulos, and A. V. Runov (2015), On the plasma sheet dependence on solar wind and substorms and its role in magnetosphere-ionosphere coupling. *Earth, Planets and Space*, *67*, doi: 10.1186/s40623-015-0296-x.

Sicard-Piet, A., S. Bourdarie, D. Boscher, R. H. W. Friedel, M. Thomsen, T. Goka, H. Matsumoto, and H. Koshiishi (2008), A new international geostationary electron model: IGE-2006, from 1 keV to 5.2 MeV, *Space Weather*, *6*, S07003, doi:10.1029/2007SW000368.

Terasawa, T., M. Fujimoto, T. Mukai, I. Shinohara, Y. Saito, T. Yamamoto, S. Machida, S. Kokubun, A. J. Lazarus, J. T. Steinberg, and R. P. Lepping (1997), Solar wind control of density and temperature in the near-Earth plasma sheet: WIND/GEOTAIL collaboration, *Geophys. Res. Lett.*, *24*, 8, 935-938, doi: 10.1029/96GL04018.

Thomsen, M. F.,M. G.Henderson, and V. K. Jordanova (2013), Statistical properties of the surface-charging environment at geosynchronous orbit, *Space Weather*, *11*, 237244, doi:10.1002/swe.20049.

Tsyganenko, N. A., and T. Mukai (2003), Tail plasma sheet models derived from Geotail particle data, *J. Geophys. Res.*, *108*, 1136, doi:10.1029/2002JA009707, A3.

Tsyganenko, N. A., and D. H. Fairfield (2004), Global shape of the magnetotail current sheet as derived from Geotail and Polar data, *J. Geophys. Res.*, *109*, A03218, doi:10.1029/2003JA010062.

Wang, C.-P., L. R. Lyons, J. M. Weygand, T. Nagai, and R. W. McEntire (2006), Equatorial distributions of the plasma sheet ions, their electric and magnetic drifts, and magnetic fields under different interplanetary magnetic field Bz conditions, *J. Geophys. Res.*, *111*, A04215, doi:10.1029/2005JA011545.

Wang, C.-P., L. R. Lyons, T. Nagai, J. M. Weygand, and R. W. McEntire (2007), Sources, transport, and distributions of plasma sheet ions and electrons and dependences on interplanetary parameters under northward interplanetary magnetic field, *J. Geophys.*

Res., *112*, A10224, doi:10.1029/2007JA012522.

Wang, C.-P., L. R. Lyons, T. Nagai, J. M. Weygand, and A. T. Y. Lui (2010), Evolution of plasma sheet particle content under different interplanetary magnetic field conditions, *J. Geophys. Res.*, *115*, A06210, doi:10.1029/2009JA015028.

Wang, C.-P., M. Gkioulidou, L. R. Lyons, and V. Angelopoulos (2012), Spatial distributions of the ion to electron temperature ratio in the magnetosheath and plasma sheet, *J. Geophys. Res.*, *117*, A08215, doi:10.1029/2012JA017658.

Wing, S., and P. T. Newell, 2D plasma sheet ion density and temperature profiles for northward and southward IMF, *Geophys. Res. Lett.*, *29(9)*, doi:10.1029/2001GL013950, 2002.

Wing, S., J. R. Johnson, P. T. Newell, and C.-I. Meng (2005), Dawn-dusk asymmetries, ion spectra, and sources in the northward interplanetary magnetic field plasma sheet, *J. Geophys. Res.*, *110*, A08205, doi:10.1029/2005JA011086.

Åsnes, A., M. G. G. T. Taylor, A.L. Borg, B. Lavraud, R.W.H. Friedel, C.P. Escoubet, H. Laakso, P. Daly, and A.N. Fazakerley (2008), Multispacecraft observation of electron beam in reconnection region, *J.* Geophys. Res., *1*13, A07S30, DOI: 10.1029/2007JA012770.

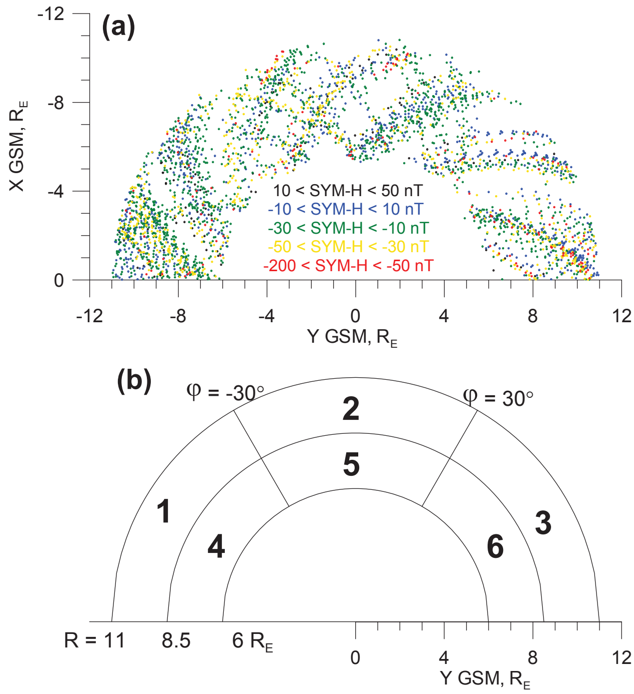

Figure 1. (a) Spatial coverage of the equatorial magnetosphere by THEMIS observations. Only every twentieth point is shown. Color shows corresponding SYM-H. (b) Spatial bins numeration.

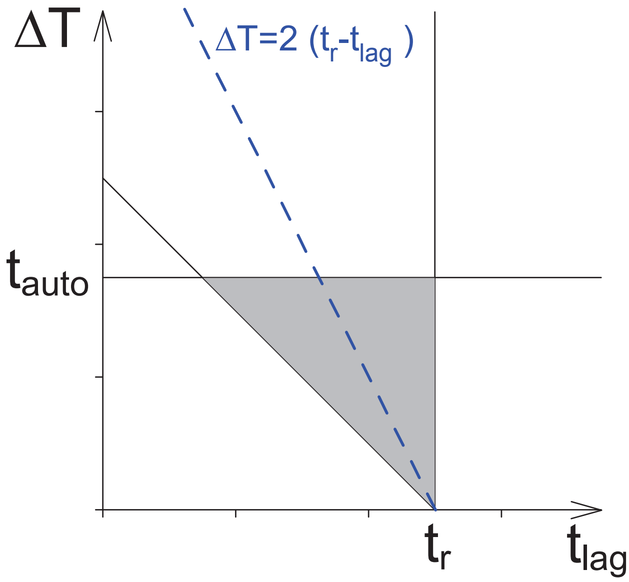

Figure 2. Sketch explaining how to interpret Figures 3–7.

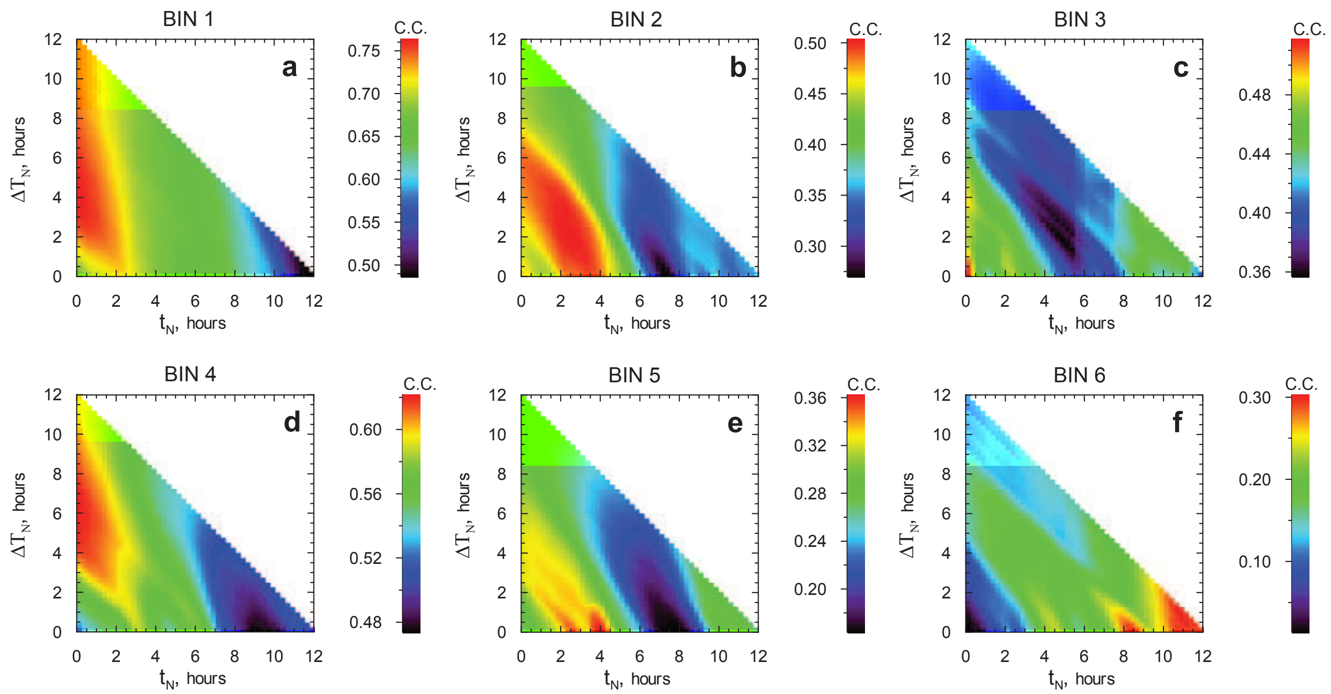

Figure 3. Correlation coefficients (color coded) between the plasma sheet electron density and solar wind density for six regions of the magnetotail. Vertical and horizontal axes show a solar wind density average duration and a lag of the solar wind density observations with respect to plasma sheet measurements.

Table 1. Statistical properties of the data sets for different spatial bins. Top part is for instant values corresponding zero lag, and the bottom part shows the ranges of standard deviations found for lags between 0 and 12 h.

Bin index	1	2	3	4	5	6
r, $[R_E]$	8.5–11	8.5–11	8.5–11	6–8.5	6–8.5	6–8.5
ϕ	$-90°$–$-30°$	$-30°$–$30°$	$30°$–$90°$	$-90°$–$-30°$	$-30°$–$30°$	$30°$–$90°$
#	18749	12082	11330	10547	9706	7873
σN_{SW}, [cm^{-3}]	5.1	3.6	4.6	5.7	4.4	5.1
σV_{SW}, km/s	119	107	93	114	107	94
σB_{ZIMF}, nT	3.9	3.7	3.4	4.2	3.7	3.6
σN_{SW}, [cm^{-3}]	4.5–6.1	3.6–5.3	3.0–4.6	5.3–8.6	3.2–7.2	3.0–5.1
σV_{SW}, km/s	117–121	104–110	92–97	112–119	106–110	94–102

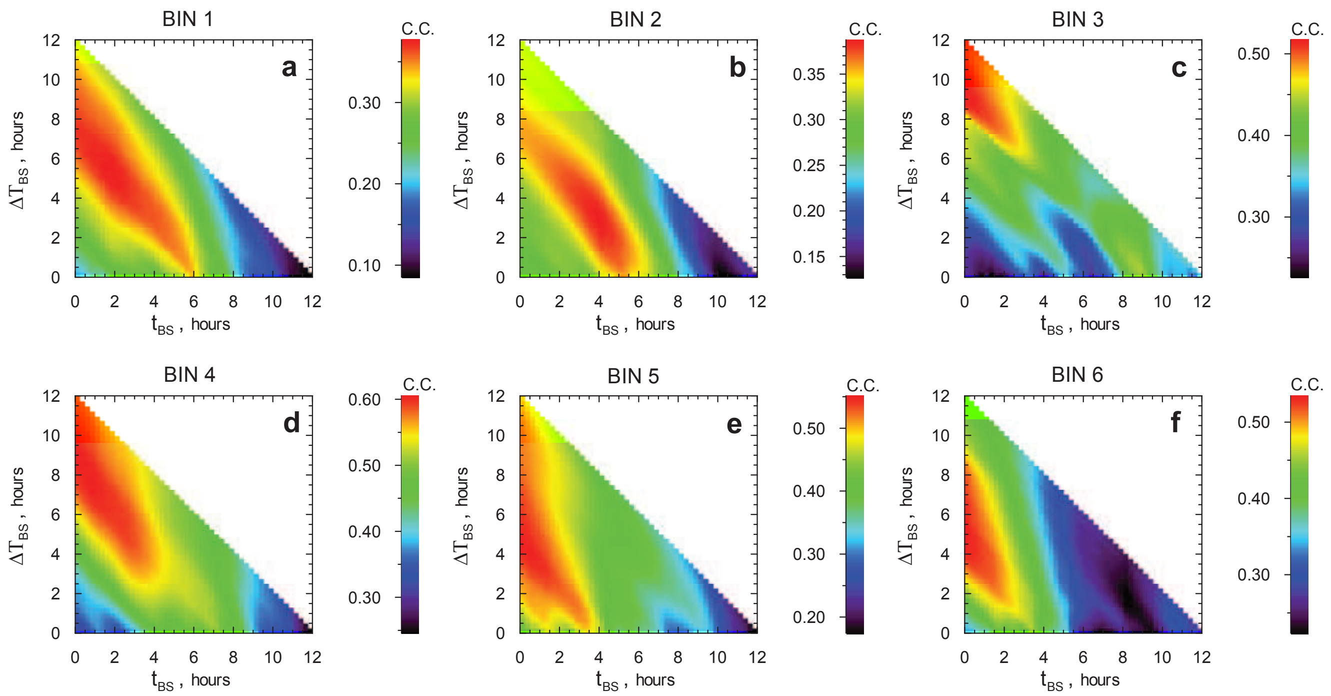

Figure 4. The same as Figure 3 but for correlation coefficients between the plasma sheet electron density and southward component of IMF B_Z.

Table 2. Correlations of the plasma sheet electron density with solar wind parameters. Top part is for instant values $t_0 - 45$ min. and the bottom part shows best correlations found for all lags and durations of averaging.

Bin index	1	2	3	4	5	6
N_{SW}	0.70	0.45	0.46	0.54	0.29	0.02
IMF B_S	0.21	0.28	0.25	0.33	0.45	0.36
IMF B_N	0.22	0.13	0.28	0.01	-0.01	0.06
N_{SW}	0.76	0.50	0.52	0.62	0.36	0.30
IMF B_S	0.38	0.39	0.52	0.61	0.55	0.53
IMF B_N	0.21	0.20	0.33	-0.27	0.13	0.12

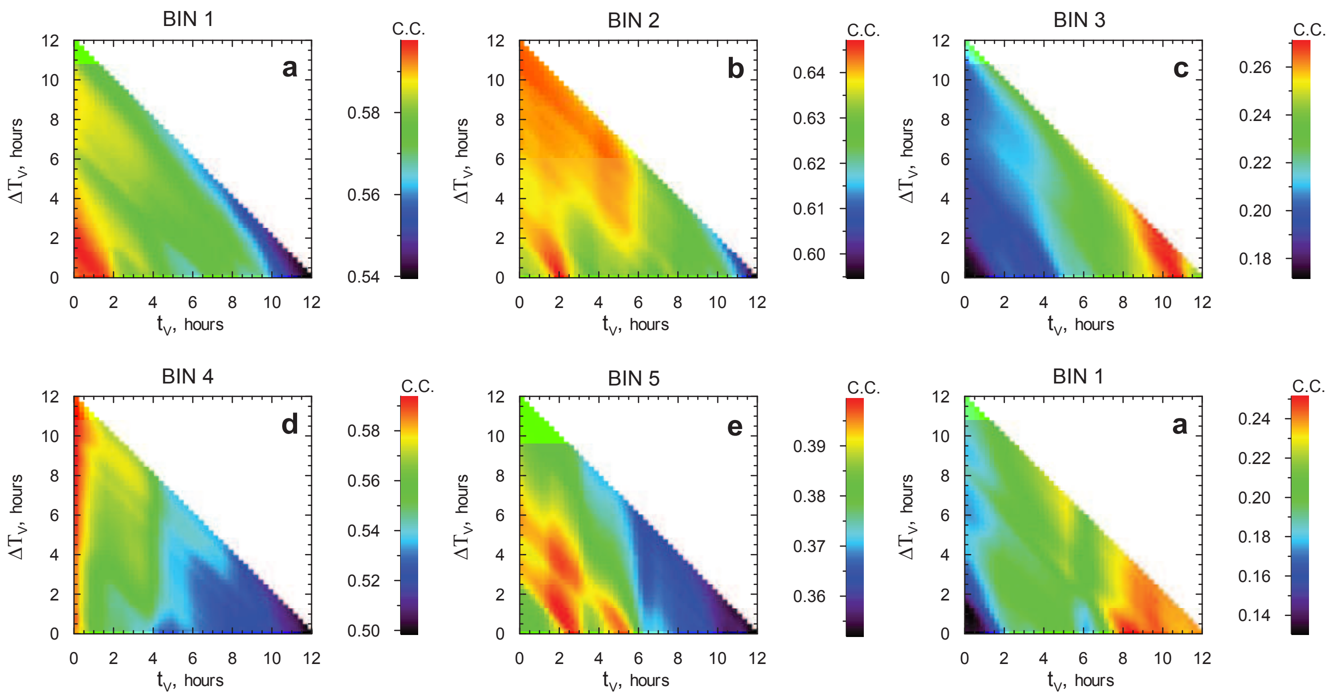

Figure 5. The same as Figure 3 but for correlation coefficients between the plasma sheet electron temperature and solar wind velocity.

Table 3. Correlations of the plasma sheet electron temperature with solar wind parameters. Top part is for instant values $t_0 - 45$ min. and the bottom part shows best correlations found for all lags and durations of averaging.

Bin index	1	2	3	4	5	6
V_{SW}	0.59	0.63	0.18	0.57	0.38	0.14
IMF B_S	0.17	0.33	0.03	0.29	0.15	-0.06
IMF B_N	-0.35	-0.30	-0.18	-0.35	-0.27	-0.14
V_{SW}	0.60	0.65	0.27	0.59	0.40	0.25
IMF B_S	0.19	0.35	-0.16	0.34	0.22	-0.14
IMF B_N	-0.41	-0.32	-0.23	-0.46	-0.28	-0.28

Table 4. Time constants for computation of the empirical models input parameters.

	t_N	ΔT_N	t_{BS}	ΔT_{BS}	t_V	ΔT_V	t_{BN}	ΔT_{BN}
Density	1.58 h	3.50 h	1.33 h	5.50 h				
Temperature			0.58 h	0.75 h	0.58 h	1.00 h	0.58 h	2.00 h

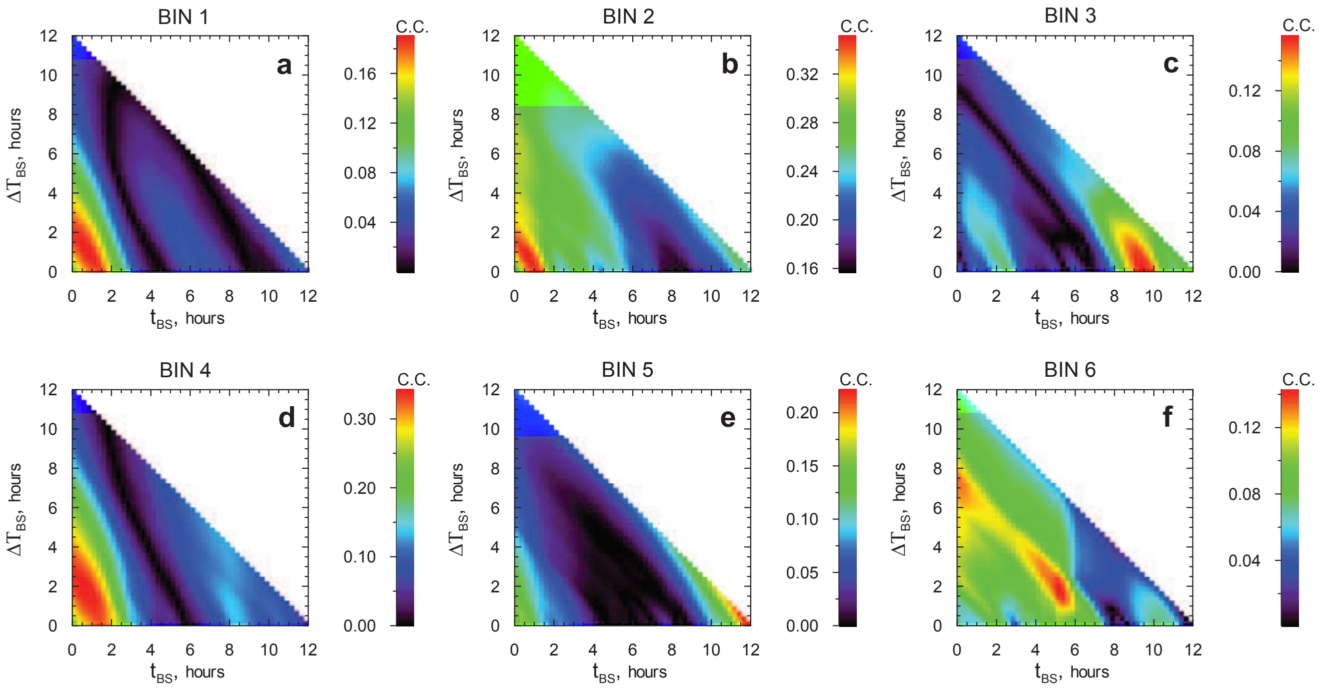

Figure 6. The same as Figure 3 but for correlation coefficients between the plasma sheet electron temperature and southward component of IMF B_Z.

Table 5. Empirical model parameters

	A_1	A_2	A_3	A_4	A_5	A_6	A_7	A_8	A_9	A_{10}	A_{11}	A_{12}
Density	0.26	-0.13	-0.14	0.29	-0.12	1.17	-1.08	0.72				
Temperature	2.65	-2.53	0.60	-0.66	0.63	1.96	1.67	-2.52	-0.29	-0.70	0.49	0.43

Table 6. Characteristics of the empirical models quality. Top part of the table for the electron density model and the bottom one is for the temperature model

Bin index	all	1	2	3	4	5	6
r, $[R_E]$		8.5–11	8.5–11	8.5–11	6–8.5	6–8.5	6–8.5
ϕ		$-90°$–$-30°$	$-30°$–$30°$	$30°$–$90°$	$-90°$–$-30°$	$-30°$–$30°$	$30°$–$90°$
C.C.	0.76	0.77	0.66	0.45	0.78	0.63	0.59
RMS, [cm$^-$3]	0.27	0.21	0.18	0.23	0.33	0.38	0.32
MAD, [cm$^-$3]	0.18	0.14	0.13	0.16	0.23	0.29	0.24
C.C.	0.65	0.72	0.72	0.47	0.73	0.45	0.39
RMS, [keV]	2.9	2.3	3.1	2.2	2.3	3.8	3.8
MAD, [keV]	2.0	1.7	2.0	1.6	1.7	2.7	2.8

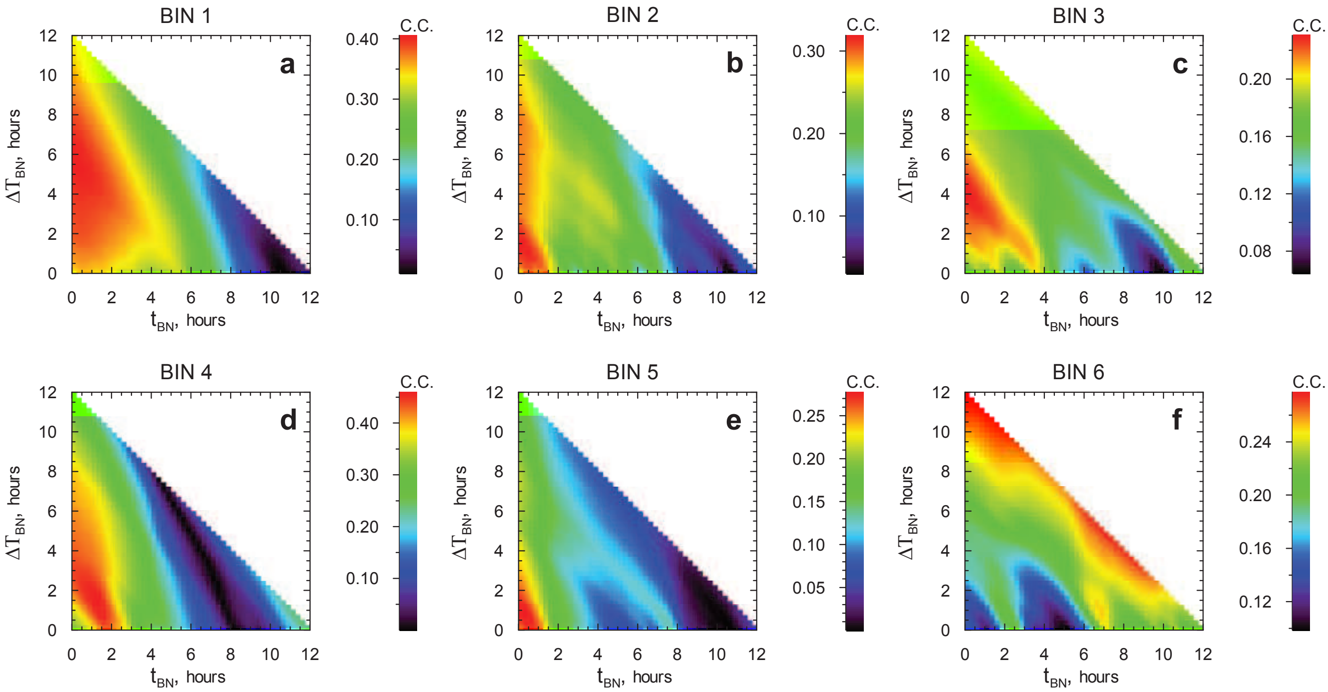

Figure 7. The same as Figure 3 but for correlation coefficients between the plasma sheet electron temperature and northward component of IMF B_Z.

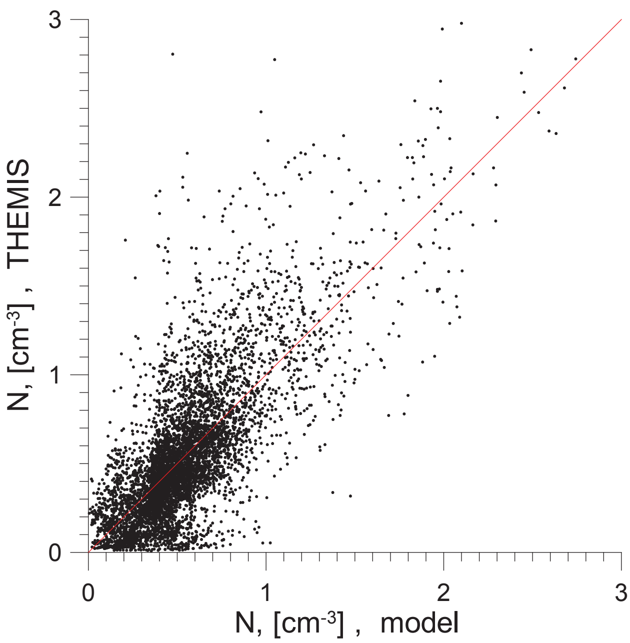

Figure 8. Plasma sheet electron density predicted by the empirical model versus that measured by THEMIS probes. Only every tenth point is shown.

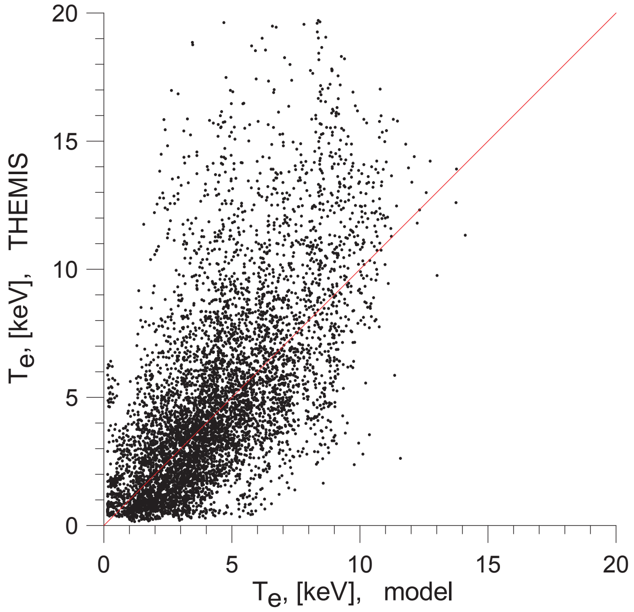

Figure 9. Plasma sheet electron temperature predicted by the empirical model versus that measured by THEMIS probes. Only every tenth point is shown.